

## 10. FLUID OVERPRESSURES IN WESTERN MEDITERRANEAN SEDIMENTS, SITES 974–979<sup>1</sup>

André Revil,<sup>2,3</sup> Philippe A. Pezard,<sup>3,4</sup> and François-Dominique de Larouzière<sup>4,5</sup>

### ABSTRACT

A compaction model was developed and applied to five sites drilled as part as Ocean Drilling Program Leg 161, during which overpressured sediments were cored. The long-term compaction coefficient for the porosity variation is very high ( $1.3\text{--}3.4 \times 10^{-7} \text{ Pa}^{-1}$ ). Assuming that the fluid overpressures result from disequilibrium compaction, the fluid overpressures can be estimated from the difference between the hydrostatic porosity (i.e., the porosity distribution that would have resulted at equilibrium compaction with hydrostatic pore-fluid pressures) and the porosity deduced from downhole measurement analysis. Fluid overpressuring starts at very shallow depths (120–150 m below seafloor) and, in some cases, very quickly reaches the reduced lithostatic pressure. The reduced lithostatic pressure corresponds to the upper limit of pore-fluid overpressure before which natural fracturing occurs in unconsolidated sediments. Fluid overpressure is commonly correlated with the presence of gas (mostly methane). The ingredients for capillary sealing, two fluid phases in a layered sequence of fine and coarse sediments, exist in all the sedimentary sections described in this paper, and layers filled with free gas are clearly revealed as spikes in the porosity derived from the density log. Capillary sealing is shown to be quantitatively capable of retaining the overpressures observed.

### INTRODUCTION

The knowledge of sediment porosity and how it changes with burial is important to uncompact sediments and to calculate sedimentation rates (Magara, 1978), to evaluate the amount of pore water that has been expelled from the sediments (Cathles and Smith, 1983), and to determine the storage capacity and permeability of hydrocarbon reservoirs (Bradley and Powley, 1994). In sedimentary basins, porosity typically decreases in a regular fashion with depth as long as the pore fluid remains hydrostatically pressured (Maxwell, 1964). Such a phenomenon is called “equilibrium compaction.” Disequilibrium compaction refers to the situation in which sediments are unable to expel their pore fluids in response to sediment loading, which causes fluid overpressure (i.e., fluid pressure in excess of hydrostatic; Magara, 1978). Under these circumstances, porosity is directly related to the effective stress, which is defined as the difference between the total confining stress and the total fluid pore pressure (Fertl, 1976; Bangs et al., 1990; Shi and Wang, 1988). Because the total stress is related simply to depth, the pore-fluid pressure can be predicted from density-log-derived porosity (Magara, 1978).

Highly pressured sediments were cored in the western Mediterranean during Ocean Drilling Program (ODP) Leg 161, requiring the scientific party to modify the usual ODP sampling strategy. To avoid explosions on the catwalk, small holes had to be drilled every 10 cm in the PVC liner along the length of each core. Frequently, a jet of water and sediments several meters high was generated as the sediment decompressed when these small pressure-release holes were drilled. The purpose of this work is to analyze the porosity distribution at several of the Leg 161 sites (Sites 974–979) to derive the compaction coefficient of the sediments and the depth distribution of pore-fluid overpressures. The fluid pressure variations in the Western Mediter-

anean Sea provide well-documented field examples of overpressured and undercompacted sediments at shallow depths that cannot be easily explained by disequilibrium compaction unless some sort of seal is present. These seals are correlated with the presence of free methane and lithologic variations in the granulometry of the sediment. A capillary sealing mechanism can explain the observed fluid overpressures. The conditions for such a seal exist at the seal location.

### SITE DESCRIPTIONS

Site 974 is located in the central Tyrrhenian Sea, halfway between continental Italy and Sardinia (water depth: 3454.0 m; Fig. 1). Sedimentary sequences compose Pliocene–Pleistocene hemipelagic deposits, with many organic-rich layers and volcanic-ash layers interbedded in the sedimentary sequence. Sedimentation rates uncorrected for compaction determined on board ship (Hole 974B) are 55.1 m/m.y. for the Holocene–Pleistocene, 27 m/m.y. for the late Pliocene, and 52 m/m.y. for the early Pliocene. Low methane concentration was observed. The first unit at Site 974 (~0–90 meters below seafloor [mbsf]) is composed of Pliocene–Pleistocene hemipelagic deposits (nanofossil-rich clay to nanofossil-rich silty clay), which are locally bioturbated. Carbonate content within this unit averages 30% by weight, and the presence of degraded marine algal and microbial material was noted (Shipboard Scientific Party, 1996a). Numerous ash and volcanoclastic layers exist, both ranging from a few millimeters to ~10–30 cm in thickness. The second unit (~90–200 mbsf in Holes 974 B and 974C, and 90–163 mbsf in Hole 974D) is composed of a Pliocene nanofossil clay and nanofossil ooze with a minor amount of foraminifers. The carbonate content averages 50 wt%. A few ash beds and a small amount of disseminated degraded organic matter are present in this unit. The sediments of both units are interpreted to have accumulated in an open-marine environment with a periodic influx of pyroclastic material (Shipboard Scientific Party, 1996a).

Site 975 is located on the South Balearic Margin (see Fig. 1), at a water depth of 2415.0 m. Two of the four holes drilled at this site reached the top of the Miocene (Messinian) evaporites. The Pliocene–Pleistocene sediments are nanofossil rich, or calcareous clays, silts, and ooze, with carbonate content increasing with depth. Thirty-seven organic-rich layers were found in the Pleistocene–

<sup>1</sup>Zahn, R., Comas, M.C., and Klaus, A. (Eds.), 1999. *Proc. ODP, Sci. Results*, 161: College Station, TX (Ocean Drilling Program).

<sup>2</sup>Cornell University, Department of Geological Sciences, 14853 Ithaca, NY, U.S.A. [revil@lmf-aix.gulliver.fr](mailto:revil@lmf-aix.gulliver.fr)

<sup>3</sup>CEREGE, CNRS, Dept. Geophysics, BP 80, 13545 Aix-en-Provence, Cedex 4, France.

<sup>4</sup>Laboratoire de Mesures en Forage, ODP-NEB, BP 72, 13545 Aix-en-Provence, Cedex 4, France.

<sup>5</sup>GAIA, 16 Bd. Notre-Dame, 13006, Marseille, France.

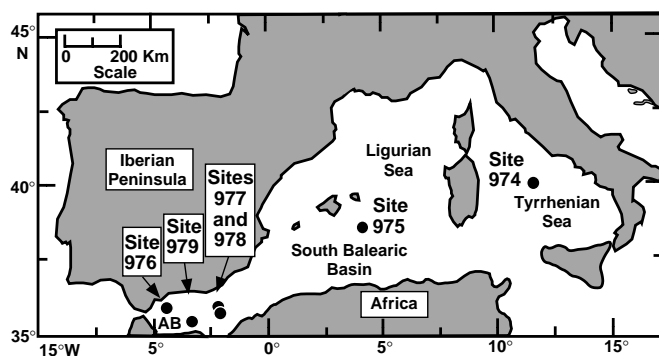


Figure 1. Map of the western Mediterranean, with the locations of Sites 974 to 979 drilled during Leg 161 (AB = Alboran Basin).

Pliocene sediments. Sedimentation rates, uncorrected for compaction, determined on board (Hole 975B) are 68 m/m.y. for the Holocene–Pleistocene, 49 m/m.y. for the late Pliocene, and 54 m/m.y. for the early Pliocene. The sedimentary formations at this site are composed of Pliocene–Pleistocene unconsolidated or poorly consolidated clay, silt, and marly ooze. The section is composed of nannofossil or calcareous clay (~60% of the section), nannofossil or calcareous silty clay (~20%), and nannofossil ooze (~20%). Carbonate content in the sediment varies between 30% and 70% and increases slightly with depth. The terrigenous sediment fraction includes mainly clay minerals (illite, kaolinite or chlorite, and smectite), and quartz. Bioturbation is common at depths >150 mbsf. Cyclic alternation of nannofossil clay to nannofossil ooze (which contains more silt- and sand-sized grains, primarily foraminifers) and darker nannofossil clay were noted. These cycles vary in thickness on a centimeter to meter scale. Some rare laminae and thin beds (<3 cm thick) rich in silt and/or sand were found at Site 975. The sediment was deposited in a tectonically inactive, open-marine environment (Shipboard Scientific Party, 1996b). The presence of gas, methane, is observed in the density log and the acoustic downhole measurements. However, the overall gas concentration throughout the section is very low at Site 975 compared with the other sites investigated because the concentration of sulfate, which inhibits methanogenesis, remains high throughout the section (Shipboard Scientific Party, 1996b). There is no trace of erosion in this section.

Site 976 is situated in the Western Alboran Sea (Fig. 1), 60 km off the coast of Spain and 110 km east of the Strait of Gibraltar (water depth: 1108.0 m). Deep holes were drilled at this site, some of them penetrating the metamorphic basement. In Hole 976B, the entire 650-m-thick sedimentary sequence was cored, covering middle Miocene–Holocene times. Very high sedimentation rates, uncorrected for compaction, were determined on board (Hole 976B), with a mean value of 208 m/m.y. for the Holocene–Pleistocene, 340 m/m.y. for the late Pliocene, 453 m/m.y. for the early Pliocene (possibly resulting from the lack of biostratigraphic control), and 15 m/m.y. for the late Miocene. The sediments at Hole 976B between 0 and 362.1 mbsf are composed of Holocene–Pleistocene open-marine hemipelagic facies of nannofossil-rich clay, nannofossil clay, and nannofossil silty clay. Continuous and discontinuous clayey silt laminae occur irregularly throughout. The carbonate content averages 28% in this unit in Hole 976B and consists of nannofossils, foraminifers, bioclasts, micrite, inorganic calcite, and dolomite. Laminated beds of diatomaceous ooze up to 5 cm thick are also observed. Downhole variations in detrital siliclastic content suggest that this unit contains three major cycles of upward-increasing terrigenous input. Twenty-eight organic-rich layers consisting mainly of nannofossil clay to nannofossil-rich clay were also observed.

Site 977 penetrated 598.5 m of Miocene(?)–Pliocene–Holocene sediments, south of Cabo de Gata in southeastern Spain (water depth: 1984.0 m; Fig. 1). Organic-rich layers are common in the Pliocene–

Pleistocene sequences. Sedimentation rates, uncorrected for compaction, were determined on board (Hole 977A), with a mean value of 154 m/m.y. for the Holocene–Pleistocene, 96 m/m.y. for the Pliocene (to an unconformity), and >400 m/m.y. below. High methane concentrations were measured in these sediments, in the range  $1.5\text{--}3.5 \times 10^4$  ppm between 100 and 450 mbsf (Shipboard Scientific Party, 1996c). The sedimentary sequence drilled at Site 977 was subdivided into two lithostratigraphic units on the basis of downhole changes in sedimentary structure and grain size. The first unit (0–532.9 mbsf) contains Holocene–Pleistocene sediments that comprise an open-marine hemipelagic facies consisting predominantly of nannofossil clay to nannofossil-rich clay, slightly to moderately bioturbated. Carbonate content ranges from 21% to 61% and consists of nannofossils, micrite, bioclasts, and foraminifers. Minor lithologies include diatoms, nannofossil ooze, and nannofossil-rich diatomaceous sandy silty clay. Sand- and silt-rich layers are intercalated with the clay-rich sediment. Sharp basal contacts are common, and intervals of slumping are found throughout this unit. The second sedimentary unit (532.9–598.5 mbsf) is formed by partly cemented sandy gravel. The gravel consists predominantly of volcanic clasts (essentially rhyodacite) and a few sedimentary clasts (dolomitic mudstone and quartz sandstone cemented by quartz and chlorite). They are coated by a calcareous cement, which suggests that the clasts were derived from the partly cemented sandy gravel.

Site 979 is located in the Southern Alboran Basin (Fig. 1), between Alboran Island and the Moroccan coast, and was drilled to a total depth of 580.9 mbsf (water depth: 1062.1 m). The deepest sediment drilled is late Pliocene in age. Average sedimentation rates, uncorrected for compaction, determined on board (Hole 979A) were 200 m/m.y. for the Pleistocene and ~187 m/m.y. for the late Pliocene. As for the other sites in the Western Alboran, high-methane concentrations were measured in the sedimentary sequence of Hole 979A in the range  $0.5\text{--}1.0 \times 10^4$  ppm (Shipboard Scientific Party, 1996d). The sediments drilled in Hole 979A were quite uniform, and only one lithologic unit was described. The sediment comprises Pleistocene–Pliocene open-marine hemipelagic nannofossil clay with minor siliclastic detrital layers. Shell fragments and dispersed silt-sized foraminifers are variably present. Bioturbation is common, but varies in intensity throughout the section. Silty and sandy turbidites occur throughout the sequence. An apparent unconformity was identified between 475 and 477 mbsf and is marked by a weakly bioturbated to structureless nannofossil-rich clay (Shipboard Scientific Party, 1996d). However, the evidence for the existence of this unconformity is weak (W. Ussler, pers. comm., 1997).

## COMPACTION MODEL

In sedimentary basins, the porosity of the sediment decreases in a regular fashion with depth as long as the pore fluid remains hydrostatic. The relationship between porosity and effective stress variations is derived in the following manner. We define a long-term porosity compressibility by:

$$\beta \equiv -\frac{1}{\phi_0} \left( \frac{d\phi}{d\sigma_{eff}} \right), \quad (1)$$

where  $\phi$  is the total interconnected porosity,  $\phi_0$  is the porosity in an uncompacted reference state corresponding to the seafloor in sedimentary basins,  $\sigma_{eff} = \sigma - p$ ,  $\sigma$  is the total confining stress, which is the first invariant of the total stress tensor, and  $p$  is the total fluid pressure (equal to the hydrostatic fluid pressure,  $p_H$ , plus a fluid overpressure term,  $\delta p$ ). Palciauskas and Domenico (1989) show that compaction by pressure solution in sedimentary basins is irreversible and several orders of magnitude more effective than the corresponding poro-elastic (reversible) compressibility. They also show theoretically that  $\beta$  does not depend on the effective stress itself. We can recast Equation 1 in the following form:

$$d\phi = -\beta\phi_0 d\sigma_{eff} \text{ as } d\sigma_{eff} \geq 0, \quad (2)$$

where  $\beta$  will be considered as a constant as shown by Palciauskas and Domenico (1989). In the following, we will consider  $\sigma_{eff} \approx (P - p)$  where  $P$  is the lithostatic stress. This approximation is valid only in absence of strong tectonic stresses, and with a Poisson's ratio close to 0.50 (Magara, 1978). The Poisson ratio for long-term deformation of mud or unconsolidated sediments such as observed at the sites investigated is close to 0.50 (Hamilton, 1971). The change in lithostatic and fluid pressures under hydrostatic conditions (subscript  $H$ ) over a depth increment  $dz$  are given by (Magara, 1978):

$$dP_H(z) = [\rho_m(1 - \phi_H) + \rho_f\phi_H]gz, \text{ and} \quad (3)$$

$$dp_H(z) = \rho_f gz, \quad (4)$$

where  $\phi_H$  is the "hydrostatic porosity" (Fig. 2),  $\rho_f$  is the density of the fluid in the interconnected pore space,  $\rho_m$  is the grain density, and  $g$  is acceleration of gravity. In the presence of gas, the fluid density  $\rho_f$  can be related to the water saturation  $S_w$  and to the gas density  $\rho_g$  by  $\rho_f = S_w\rho_w + (1-S_w)\rho_g$  where  $\rho_w$  is the saline water density. Because, the differential of the effective stress is given by  $d\sigma_{eff} \equiv d\sigma - dp = dP_H - dp_H$ , Equations 3 and 4 allow the compaction equation, Equation 2, to be rewritten:

$$d\phi_H = -\phi_0 \beta g(\rho_m - \rho_f)(1 - \phi_H) dz. \quad (5)$$

Integration from the seafloor ( $z = 0, \phi = \phi_0$ ) to depth  $z$  yields:

$$\ln\left(\frac{1 - \phi_H(z)}{1 - \phi_0}\right) = \frac{z}{z_c}, \quad (6)$$

where the characteristic depth  $z_c$  is defined by:

$$z_c \equiv 1/\phi_0 \beta g(\rho_m - \rho_f). \quad (7)$$

Equation 6 can be rewritten to give:

$$\phi_H(z) = 1 - (1 - \phi_0) \exp\left(\frac{z}{z_c}\right). \quad (8)$$

Equation 8 corresponds to the normal trend of compaction in sedimentary basins. Finally, the lithostatic pressure in a hydrostatically pressured section,  $P_H$ , can be obtained by substituting Equation 8 into Equation 3 and integrating from the surface to the depth  $z$ , yielding:

$$P_H(z) = \rho_f gz + g(\rho_m - \rho_f)(1 - \phi_0)z_c \left[ \exp\left(\frac{z}{z_c}\right) - 1 \right]. \quad (9)$$

Fluid overpressure is the result of a balance between the rate of overpressure generation and its dissipation by fluid flow (Palciauskas and Domenico, 1989). In this paper, we only consider fluid overpressures resulting from disequilibrium compaction. Disequilibrium compaction refers to the situation where sediments are unable to expel their pore fluids in response to sediment loading, which causes fluid overpressure. It is convenient to describe all parameters as departures from the values these parameters would have under hydrostatic conditions. Defining the departure from hydrostatic pore pressure, lithostatic pressure, and porosity by  $\delta p$ ,  $\delta P$ , and  $\delta\phi$ , we can write the fluid pressure, the lithostatic pressure, and the porosity without loss of accuracy:

$$p = P_H + \delta p, \quad (10)$$

$$P = P_H + \delta P, \text{ and} \quad (11)$$

$$\phi = \phi_H + \delta\phi, \quad (12)$$

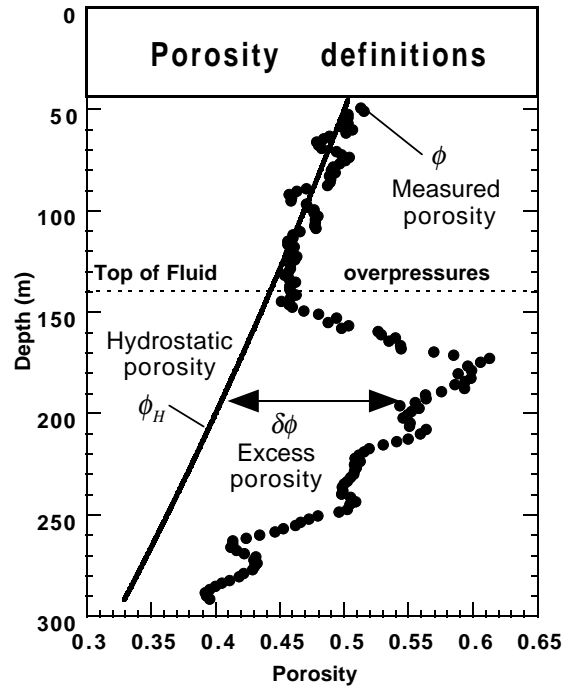


Figure 2. Definitions of the porosity parameters introduced in the model. The hydrostatic porosity distribution,  $\phi_H$ , is the porosity distribution resulting from equilibrium compaction (i.e., no pore fluid overpressures are generated). The function  $\phi_H = f(z)$  is called the "(hydrostatic) normal trend of compaction." The measured porosity,  $\phi$ , is equal to  $\phi_H$  only in the hydrostatically pressured formations. The case  $\phi > \phi_H$  corresponds to undercompacted formations. The case  $\phi < \phi_H$  corresponds to overcompacted formation. If fluid overpressures result from a compaction disequilibrium process, the difference  $\phi - \phi_H = \delta\phi$  is called the "excess porosity" and can be directly related to the fluid overpressure  $\delta p$ .

where  $p_H = \rho_f gz$  is the hydrostatic fluid pressure, and  $P_H$  and  $\phi_H$  are given by Equations 8 and 9, respectively. We call  $\delta\phi$  the "excess porosity" (Fig. 2). From Equations 2, 10, 11, and 12, the porosity change  $\delta\phi$  is related to the effective stress change,  $\delta P - \delta p$ , by:

$$\delta\phi = -\phi_0 \beta (\delta P - \delta p). \quad (13)$$

The lithostatic stress is related to the porosity by:

$$P(z) = g \int_0^z [\rho_m(1 - \phi) + \rho_f \phi] dz'. \quad (14)$$

Combining Equations 3, 11, 12, and 14, we have:

$$\delta P = - \int_0^z (\rho_m - \rho_f) g \delta\phi dz'. \quad (15)$$

Combining Equations 13 and 15, we see the excess fluid pressure and the excess porosity are related by:

$$\delta p(z) = \frac{\delta\phi(z)}{\phi_0 \beta} - \int_0^z (\rho_m - \rho_f) g \delta\phi(z') dz', \quad (16)$$

or alternatively, using the definition of the characteristic depth  $z_c$ , Equation 7,

$$\delta p(z) = \frac{1}{\phi_0 \beta} \left( \delta \phi(z) - \frac{1}{z_c} \int_0^z \delta \phi(z') dz' \right). \quad (17)$$

The second term of Equation 17 represents the variation of the lithostatic pressure induced by variations of the excess porosity  $\delta \phi$ . Equations 13–17 are exact in the sense that they do not result from any approximation other than the constraint of disequilibrium compaction discussed above. Provided  $\delta p \geq 0$ ,  $\delta \phi$  is necessarily positive.

Lithologic variations and, in particular, the compaction of sediments in which clay minerals mix with sand grains can be quantified for sand/shale mixtures as illustrated in Figure 3. The noncompacted porosity is obtained from the clay weight fraction,  $\phi_w$ , by:

$$\phi_0 = \begin{cases} \phi_{sd} - \frac{(1 - \phi_{sd}) \rho_{sd} \phi_w}{\rho_{sh} (1 - \phi_w)}, & \text{as } \phi_w \leq \phi_w^{\text{crit}} \\ \frac{\phi_{sh} \rho_{sd} \phi_w}{\rho_{sd} \phi_w + (1 - \phi_{sh}) \rho_{sh} (1 - \phi_w)}, & \text{as } \phi_w > \phi_w^{\text{crit}} \end{cases}. \quad (18)$$

where  $\phi_{sd}$  and  $\phi_{sh}$  ( $\rho_{sd}$  and  $\rho_{sh}$ ) are respectively the interconnected porosity (the grain density) for a noncompacted clean sand and a noncompacted pure shale. The critical shale content  $\phi_w^{\text{crit}}$ , which characterizes the boundary between the clayey sand domain and the sandy shale domain (Fig. 3), is defined by:

$$\phi_w^{\text{crit}} = \frac{\phi_{sd} (1 - \phi_{sh}) \rho_{sh}}{(1 - \phi_{sd}) \rho_{sd} + \phi_{sd} (1 - \phi_{sh}) \rho_{sh}}. \quad (19)$$

It follows from Equations 8, 18, and 19 that the porosity can be predicted completely from the knowledge of the shale content of the formations, the depth, the uncompacted porosity  $\phi_0$ , and the compressibility  $\beta$ . The uncompacted porosity and the compressibility are determined in the upper section of the sedimentary column provided that this domain is hydrostatically pressured.

The gamma-ray log is a measure of the natural radioactivity of the sediment formations, and can be used to estimate the shale content (Ellis, 1987). We assume that the clay weight fraction of the formations is given to a first order by:

$$\phi_w = \frac{\gamma - \gamma_{sd}}{\gamma_{sh} - \gamma_{sd}}, \quad (20)$$

where  $\gamma$  is the gamma-ray reading,  $\gamma_{sd}$  is the gamma-ray value of a pure sand, assumed here to be equal to ten gamma-ray units, where-

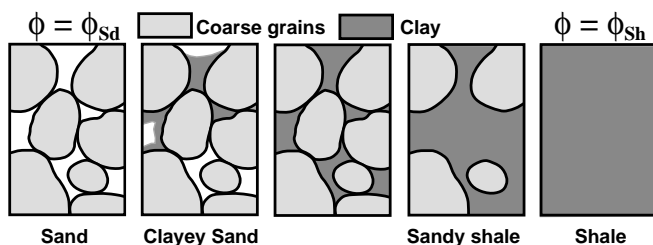


Figure 3. Sand/shale mixture model used to derive the noncompacted porosity of the formation. The porosities  $\phi_{sd}$  and  $\phi_{sh}$  are the noncompacted porosity corresponding to a clean sand and a perfect shale, respectively. The porosity is at a maximum for the two end-members of the model and is at a minimum when clays fill the pores of grain-supported sand (center panel). For the formations studied in this paper, sediments are mostly clean and clayey sands, with a high carbonate content (20%–50% by weight).

as  $\gamma_{sh}$  is the gamma-ray value of a pure shale (120 gamma-ray units). This equation should be considered as a rough approximation because (1) nonradioactive clay minerals may be present, and (2) uranium-rich formations can be interpreted as shale layers (Ellis, 1987). We assume the following:  $\rho_m = \rho_{sh} = \rho_{sd} = 2650 \text{ kg m}^{-3}$ , and  $\phi_{sd} = \phi_{sh} = 0.65$ .

## RESULTS

The first step in analyzing the downhole measurements is to determine the noncompacted porosity,  $\phi_0$ , and the long-term compressibility  $\beta$ . Only two holes can be used for this purpose (Hole 975C and Hole 974C) because both exhibit a hydrostatically pressured upper compartment. The regular decrease in porosity with the depth of burial between the seafloor and 120 mbsf in these two cases is a clear indicator that the formations are hydrostatically pressured in this depth range (Fig. 4). For these two holes only, it appears that there is no free gas phase between 0 and 120 mbsf, as indicated by the agreement between the neutron porosity log and that derived from the density log (using  $\rho = [1 - \phi] \rho_m + \phi \rho_f$ ). A nonlinear regression analysis based on Equation 8 is applied to Sites 974 and 975 (Fig. 4). The average noncompacted porosity and the characteristic depth are used in Equation 7 to calculate an average compressibility  $\beta$ . Because a free gas phase was not detected in the formations between the seafloor and 120 mbsf at these two sites, we assume that  $\rho_f = \rho_w$ . Estimates of the long-term compressibility are  $\beta = 1.41 \times 10^{-7} \text{ Pa}^{-1}$  in Hole 975C and  $\beta = 3.35 \times 10^{-7} \text{ Pa}^{-1}$  in Hole 974C. Such a difference between the compressibility coefficient computed at these two sites is not completely surprising. A. Revil and L.M. Cathles (unpubl. data) noted an excellent correlation between the long-term compressibility,  $\beta$ , and the average geothermal gradient,  $G$ , in sedimentary basins. The data reported by these authors show a very good linear correlation between the two parameters for geothermal gradients in the range  $20^\circ\text{--}40^\circ\text{C km}^{-1}$ . The geothermal gradient analyzed in Figure 5 from the equilibrium temperature distribution is two times greater in Hole 974C ( $G = 130.4^\circ\text{C km}^{-1}$ ; Fig. 5) than in Hole 975C ( $G = 62.7^\circ\text{C km}^{-1}$ , Fig. 5). To estimate  $\beta$  at the other sites where hydrostatic conditions were not observed, we used the following empirical formula relating  $\beta$  to the geothermal gradient:

$$\beta = \beta_0 [1 + \alpha (G - G_0)], \quad (21)$$

where  $\beta_0$  ( $= 1.86 \times 10^{-8} \text{ Pa}^{-1}$ ) is the long-term compressibility corresponding to a reference geothermal gradient  $G_0$  ( $20^\circ\text{C/km}$ ), and  $\alpha = 15.37 \times 10^{-2}$ . The temperature data reported by Comas, Zahn, Klaus, et al. (1996) are analyzed in Figure 5. The values of  $\alpha$  and  $\beta_0$  are calculated from the results obtained from the various holes investigated.

The compaction equation, Equation 8, can be solved using Equations 18 and 19 to test the ability of the model to reproduce both long and short length-scale porosity variations. The clay weight fraction of the formations is estimated from the gamma-ray log using Equation 20, and the noncompacted porosity is estimated from Equation 6. A test case of the model is illustrated in Figure 6. The porosity is at a maximum for the two end-members of the model (clean sand and pure shale) and at a minimum when clays fill the pores of the sand (center panel, Fig. 3). If we estimate the clay weight fraction of the formations from the gamma-ray log, we find that our compaction model is able to reproduce both long and short length-scale porosity variations (Fig. 6C). The good agreement between model and porosity data (Fig. 6C) indicates that the small-length scale porosity variations are effectively caused by lithologic variations related to shale content. In particular, the model reproduces the correlations and anticorrelations between the clay weight fraction and the porosity curve (Figs. 6A, 6B), depending on clay weight fraction (the limit being

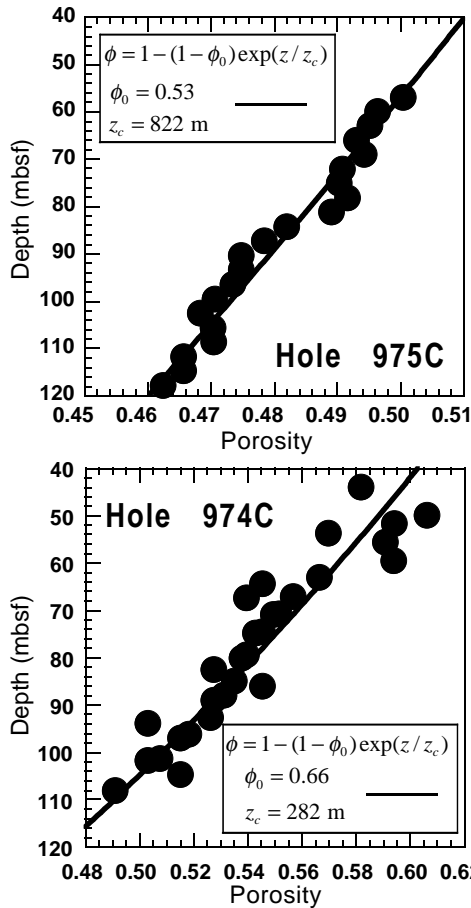


Figure 4. Determination of the noncompacted porosity and the long-term compressibility of the formations in Holes 975C and 974C. The porosity data (inferred from the density log) from the upper part of the borehole are inverted using Equation 8. Before the nonlinear regression, the data were averaged using a sliding window of 20 m. The values of the noncompacted porosity and the characteristic depth associated with equilibrium compaction are given on the graph.

$\phi_w^{\text{crit}} = 0.39$  given by Equation 19 for the clay weight fraction between the “clayey sand domain” and the “sandy shale domain”). Porosity increases with increasing clay content if the clay fraction is  $>0.39$ , but decreases with increasing clay fraction if the clay fraction is  $<0.39$ .

Downhole measurements from Leg 161 are used to estimate the sedimentation rate, taking into account the compaction effects, and fluid overpressures (Figs. 7A–7D). Using a simple mass balance argument, the uncompacted sedimentation rate,  $\omega_0$ , can be estimated with the following equation (Magara, 1978):

$$\omega_0 = \omega \left( \frac{1 - \bar{\phi}}{1 - \bar{\phi}_0} \right), \quad (22)$$

where  $\omega$  is the measured sedimentation rate between the depths  $z$  and  $(z + \delta h)$ , that is:

$$\omega \equiv \frac{\delta h}{\delta t}, \quad (23)$$

where  $\delta h$  is the difference in depth between two biostratigraphic markers, and  $\delta t$  is the age difference between the same two biostratigraphic markers. Biostratigraphic markers are based on the first or

last occurrence of calcareous nannofossils and planktonic foraminifers (Comas, Zahn, Klaus, et al., 1996). The porosities  $\bar{\phi}$  and  $\bar{\phi}_0$  are average porosity and average noncompacted porosity, respectively, between the depth  $z$  and  $(z + \delta h)$  computed using

$$\bar{\phi}(z, z + \delta h) = \frac{1}{\delta h} \int_z^{z + \delta h} \phi(z') dz', \quad \text{and} \quad (24)$$

$$\bar{\phi}_0(z, z + \delta h) = \frac{1}{\delta h} \int_z^{z + \delta h} \phi_0(z') dz'. \quad (25)$$

The porosity distribution  $\phi(z)$  is estimated from the neutron porosity log or from the density log corrected for the presence of gas. The noncompacted porosity distribution  $\phi_0(z)$  is estimated from the gamma-ray log using Equations 18–20.

The excess porosity distribution is estimated for each borehole from the difference between the normal compaction trend computed from  $\beta$  (derived from the geothermal gradient) and  $\phi_0$  (derived from the gamma-ray log). The lithostatic pressure is calculated by numerical integration of the density log and the water depth  $z_w$ :

$$P(z) = \int_0^z g \rho(z') dz' + \rho_f g z_w, \quad (26)$$

where  $\rho$  is the density distribution of the sediment with depth  $z$  below the seafloor. The reduced lithostatic pressure is defined as the lithostatic pressure  $P_R(z)$  minus the water hydrostatic pressure:

$$P_R(z) = \int_0^z g(\rho(z') - \rho_f) dz'. \quad (27)$$

Using Equation 16, the fluid overpressure can be computed from the excess porosity. Porosity profiles can be computed from the density logs using (Ellis, 1987):

$$\phi = \frac{\rho - \rho_f}{\rho_m - \rho_f}. \quad (28)$$

Because we use the approximation in  $\rho_f = \rho_w$  in Equation 28 to limit the number of unknown parameters, the presence of gas appears on the density-derived porosity as high-frequency variations (see Figs. 7A–7C). This is because the density of free gas is much smaller than the density of water. These high-frequency variations are removed before fluid overpressure is calculated. The validity of the fluid overpressure calculation from the porosity distribution and the present model has been checked by A. Revil and L.M. Cathles (unpubl. data) for sand/shale formations in the Gulf of Mexico coast, using mud weight data and borehole fluid pressure measurements. This method is valid only in the case where fluid overpressure results from disequilibrium compaction processes. In the wells presented here, the fluid overpressure estimates cannot be checked directly because direct fluid overpressure measurements were not obtained. However, because the Poisson ratio for long-term deformation of mud or unconsolidated sediments is close to 0.50 (Hamilton, 1971), the minimum horizontal stress should be close to the lithostatic load  $P$ . Consequently, the increase in fluid overpressure should be limited to the value of the reduced lithostatic stress itself. This prediction is verified in a particularly striking manner in Holes 975C and 977A (Figs. 7A, 7B).

In the case where the formations remain largely uncompacted near the surface (Holes 976B and 979A), it is also possible to compute the gas saturation using the gamma-ray log or as a combination

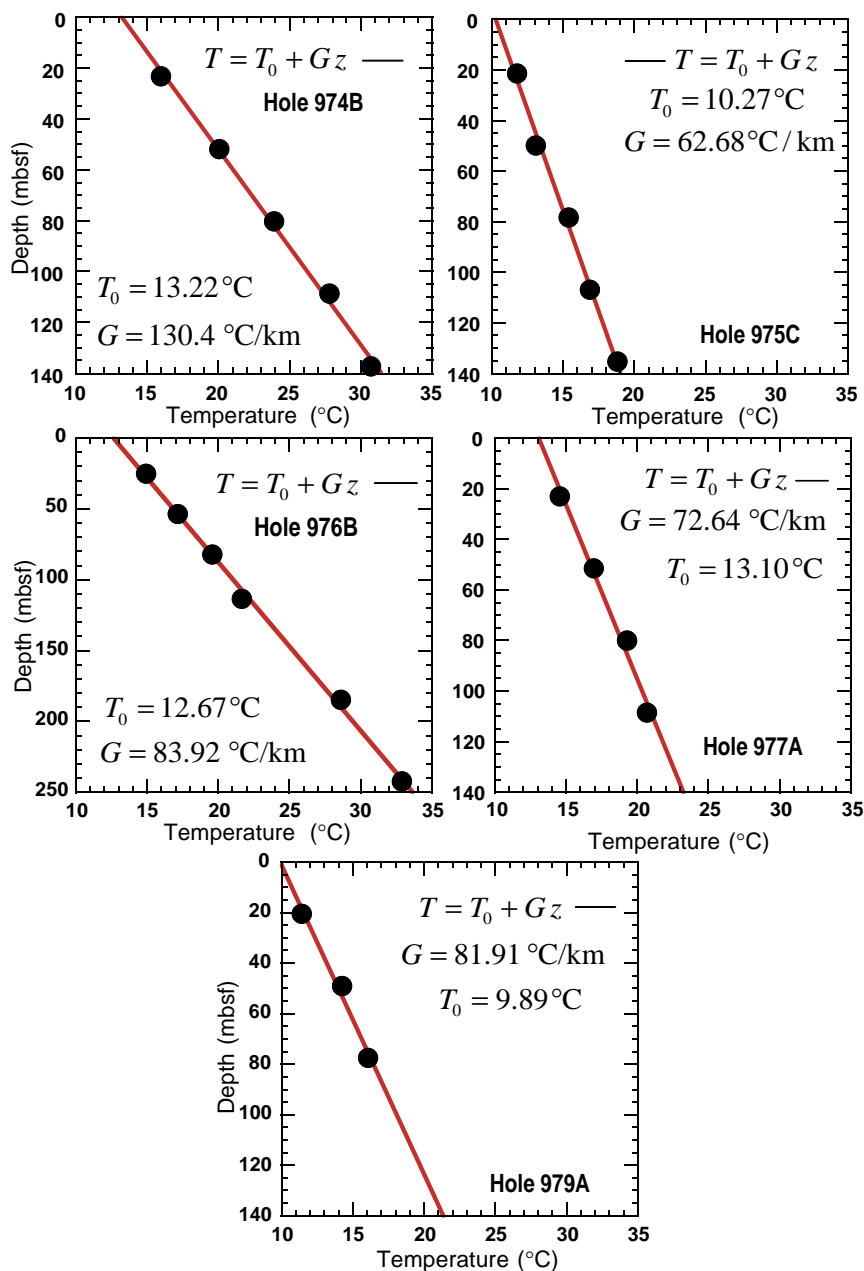


Figure 5. Equilibrium temperatures vs. depth from the ADARA and WSTP temperature sensors tool runs (data from Comas, Zahn, Klaus, et al., 1996). The seafloor temperature,  $T_0$ , and the geothermal gradient,  $G$ , are calculated from a linear regression of the data.

of the neutron porosity and the density logs. Gas saturation appears to be very high below 120 mbsf in these two boreholes (Figs. 7C, 7D).

## DISCUSSION

The high compressibility inferred from the data is probably a result of two phenomena: (1) mechanical compaction, which is usually the dominant deformation mechanism at shallow depths, and (2) compaction by pressure solution. A. Revil and L.M. Cathles (unpubl. data) reported that high geothermal gradients increase the compaction coefficient associated with pressure solution in sedimentary basins. Precipitation of high-magnesium calcite here seems to be indicated, for example, at Site 977 from magnesium and calcium concentration profiles with depth (Shipboard Scientific Party, 1996c). Authigenic calcite rhombs were observed in Cores 161-977A-2H, 3H, and 4H. Biogenic carbonate recrystallization releases strontium to the pore space (Deer et al., 1966). Carbonate recrystallization at

depth is suggested by the increase in strontium concentrations from ~100  $\mu\text{M}$  in the top 37 m to 1437  $\mu\text{M}$  at 477.7 mbsf at Site 977. Similar variations are also reported at other sites drilled during Leg 161. However, the amount of recrystallized carbonate is not significant enough to seal fluids by decreasing the intrinsic permeability of the formations. The large fluid overpressures observed in all holes inhibit, or, at least, slow down dissolution/precipitation processes by pressure solution. In the presence of high fluid pressures in the pore space, load is transferred from the grain-to-grain contacts to the fluid phase (Palciauskas and Domenico, 1989).

The observed fluid overpressures could result from disequilibrium compaction associated with the high sedimentation rates recorded in these areas (50–200 m/m.y.). The sedimentary columns analyzed form layered systems and vertical permeability is limited by the permeability of the shaly layers. However, to explain the observed fluid overpressures, the permeability should be ~1 nD. The sediments observed are not very compacted, not very cemented, and not very shaly, as shown by the gamma-ray log. Their permeability is likely to be >1 mD. Even if relative permeabilities are considered because of

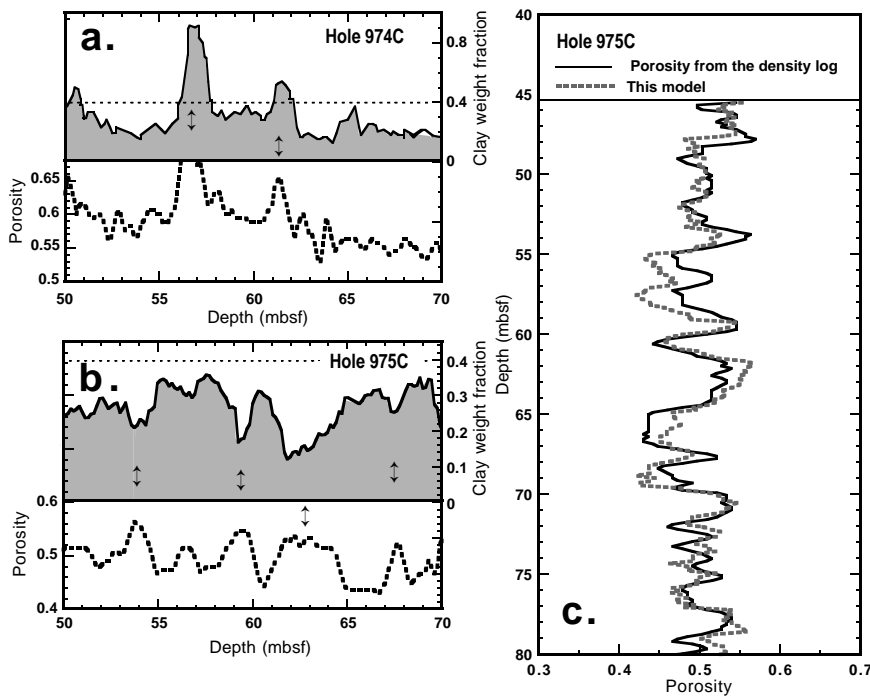


Figure 6. Selected portions of the porosity for Holes 974C (A) and 975C (B) are illustrated. Porosity is derived from the density log, and shale content is derived from the gamma-ray log. For shale content > 0.394, the model predicts that porosity and shale content are positively correlated. For shale content < 0.39, the model predicts that porosity and shale content are anticorrelated. Such correlations are observed in the diagrams (as indicated by small arrows) depending on shale content. C. The porosity can be predicted as a function of depth as the combination of two effects: (1) a high-amplitude variation, which reflects the compaction and the effects of fluid overpressure, and (2) small-scale variations caused by lithologic variations related to variations of the clay content.

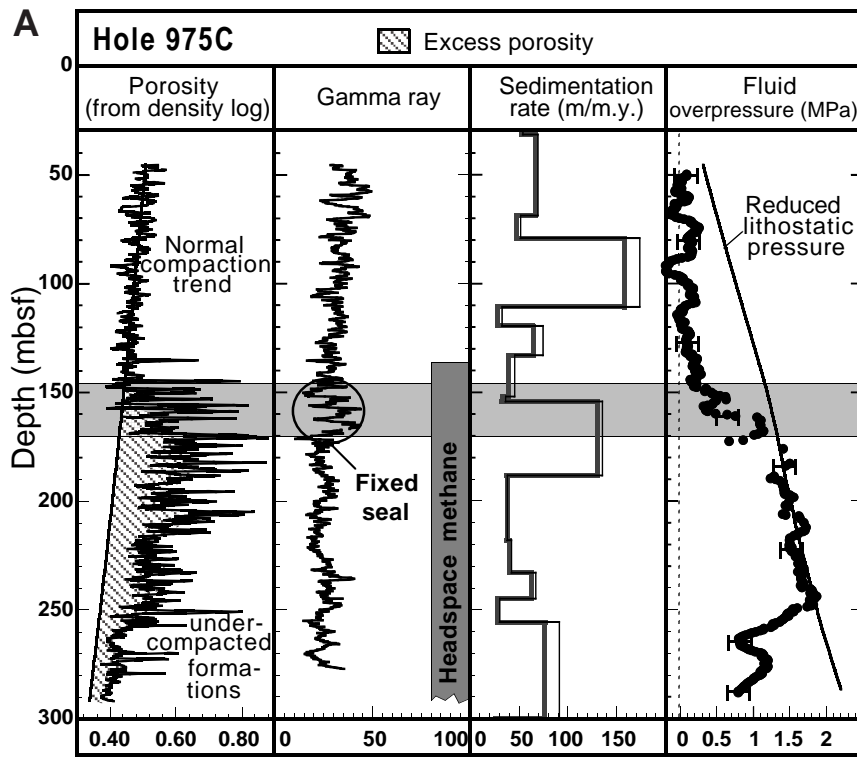


Figure 7. A. Porosity analysis from Hole 975C. The porosity derived from the density log decreases almost linearly with depth of burial from seafloor to 120–145 mbsf. Such a decrease is characteristic of equilibrium compaction, and the normal compaction trend is indicated by the plain (almost linear) curve ( $\phi_0 = 0.53$ ,  $\beta = 1.41 \times 10^{-7} \text{ Pa}^{-1}$ ). Between 145 and 170 mbsf, there is an apparent increase of the porosity with depth and, below this depth, the porosity is higher than predicted by the (hydrostatic) normal trend of compaction. This anomalous porosity (dashed zone) is not caused by lithologic variations because the gamma-ray log, an indicator of a shale content, is fairly constant. It is interpreted as the result of fluid overpressure: the porosity in the formations between 145 to 250 mbsf has been “frozen” at shallower depths because of the presence of a sealing mechanism (a “fixed seal”), probably related to the presence of gas, which is indicated by the high-frequency variations in the porosity curve below 140 mbsf (see main text). Fluid overpressure (fluid pressure above hydrostatic) is estimated from the difference between the porosity predicted by the normal compaction trend and the porosity derived from the density log. The lithostatic pressure is derived by numerical integration of the density log. The reduced lithostatic pressure is defined as the lithostatic pressure minus the hydrostatic pressure. Below the seal, the fluid overpressure is observed to be close to the reduced lithostatic pressure, which indicates the presence of natural fracturing in the transition zone. (Continued next page.)

the presence of free gas, a permeability of 1 nD would be difficult to obtain for these poorly compacted sediments. Consequently, another mechanism may be inhibiting vertical flow at the sites investigated and is responsible for the maintenance of the observed fluid overpressures.

In the case of a two-phase flow perpendicular to stratified formations consisting of alternating fine/coarse grained sediments, capillary effects can seriously affect the flow of both phases (Berg, 1975; Lenormand et al., 1994). Capillary blockage is well known in soil sci-

ences (Ross, 1990; Steenhuis et al., 1991). A capillary seal is formed when the gradient of the capillary pressure (a function of the surface tension between water, the wetting fluid for the mineral grains, and gas, the nonwetting fluid) is greater or equal than the fluid overpressure of water (Fowler, 1970). In the presence of free gas, capillary pressure drops are formed at each interface between sediments of different grain sizes. Contacts between sand- or silt-rich layers and the clay-rich sediment such as observed at many sites and the presence of free methane can generate capillary pressure drops.

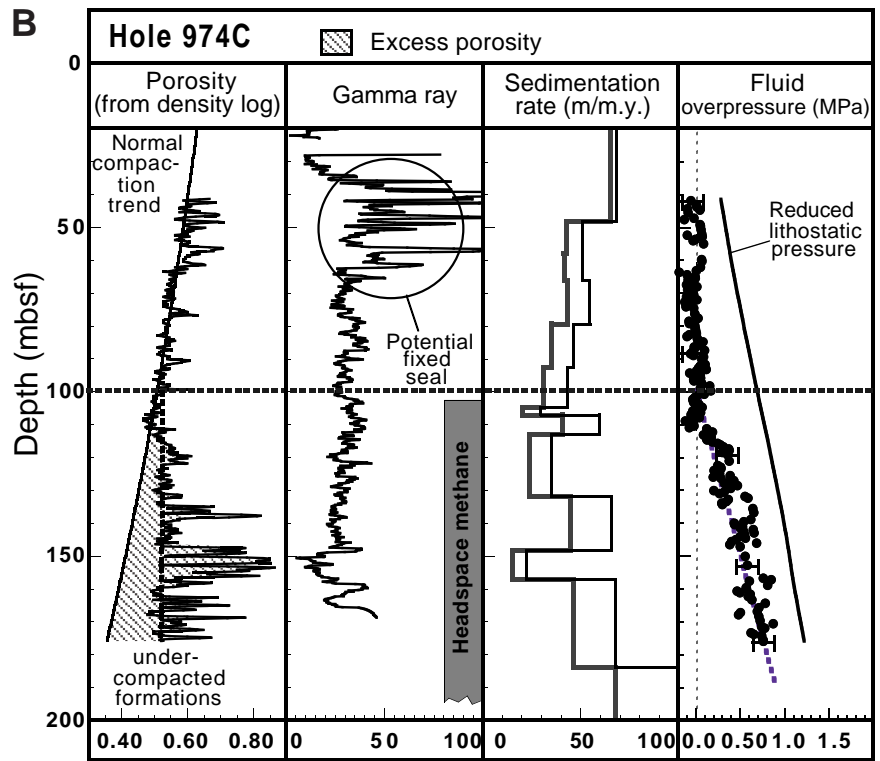
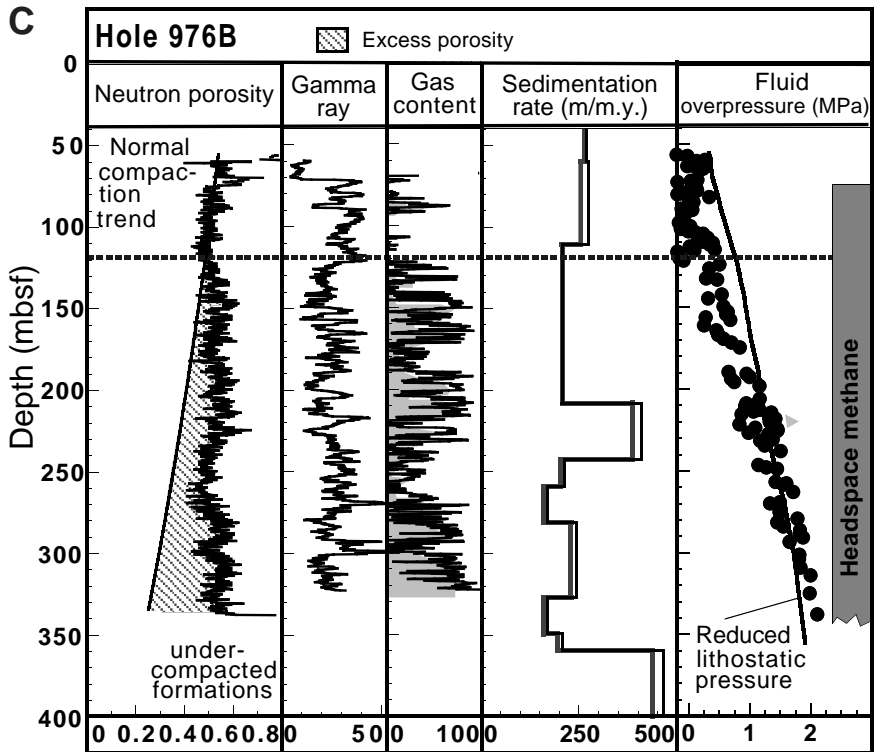


Figure 7 (continued). **B.** A porosity analysis of Hole 974C is illustrated. The porosity derived from the density log decreases almost linearly with depth of burial from 40 mbsf until reaching a transition zone at 100 mbsf. Such a decrease is characteristic of equilibrium compaction and the normal compaction trend is indicated by the solid (almost linear) curve ( $\phi_0 = 0.66$ ,  $\beta = 3.35 \times 10^{-7} \text{ Pa}^{-1}$ ). Below 100 mbsf, the porosity remains constant with depth. The high-frequency porosity variations below 120 mbsf are artificial and result from the presence of gas that has not been accounted for when porosity was derived from the density log. The constant porosity trend below 100 mbsf is characteristic of a migrating seal: the top of the undercompacted domain is not fixed in a framework attached to the sediments, but is fixed in a framework attached to the seafloor (A. Revil and L. Cathles, unpubl. data). Fluid overpressure is estimated from the excess porosity. Below 110 mbsf, fluid overpressure increases linearly with depth. **C.** A porosity analysis of Hole 976B is illustrated. From 60 to 120 mbsf, the porosity seems to follow the normal trend of compaction. Below 120 mbsf, the porosity remains relatively constant with depth. The porosity trend below 120 mbsf is characteristic of a migrating seal. The gas saturation (in weight) can be estimated from a combination between the neutron porosity and density logs. The gas saturation is very high. The shale content determined from the gamma-ray log (see main text) indicates no significant sand/shale ratio variation. The fluid overpressure increases almost linearly with depth until it reaches the fracture limit. Parameters used:  $\phi_0 = 0.58$ ,  $\beta = 1.84 \times 10^{-7} \text{ Pa}^{-1}$ . (Continued next page.)



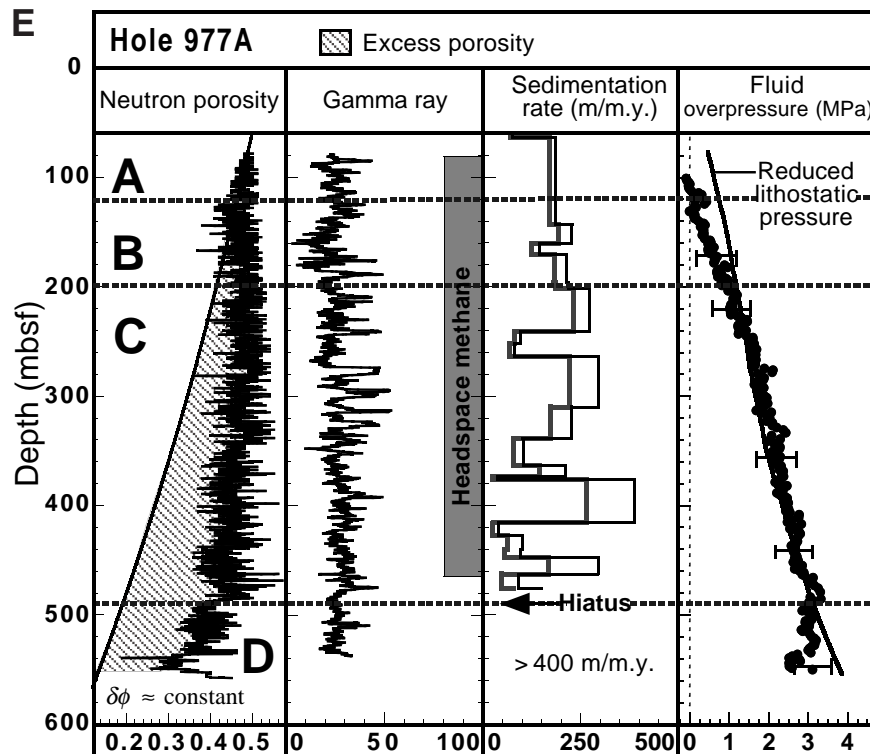
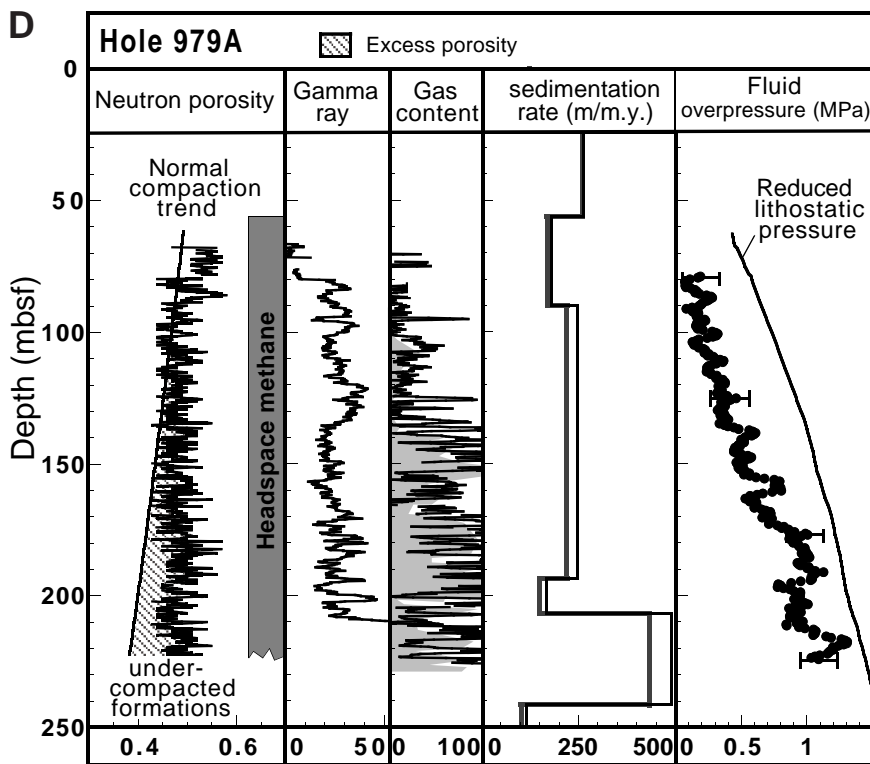


Figure 7 (continued). **D.** A porosity analysis of Hole 979A is illustrated. The neutron porosity remains relatively constant with depth. The shale content (determined from the gamma-ray log, see main text) indicates no significant sand/shale ratio variations. The fluid overpressure increases almost linearly with depth. **E.** A porosity analysis from Hole 977A is illustrated. The excess porosity computed from the neutron porosity indicates that the sediments at this site are largely undercompacted. Four compartments can be observed (A–D). A corresponds to a hydrostatic compartment. Between 120 mbsf and 200 mbsf (compartment B), the fluid overpressure increases linearly with depth. Between 200 and 485 mbsf (compartment C), the decrease in porosity with depth seems to be related to the fact that the fracture limit is reached (the fluid overpressure cannot exceed the reduced lithostatic stress). Below 485 mbsf, the excess porosity and the fluid overpressure remain constant with depth. The boundary between compartments C and D is correlated to a hiatus in the stratigraphic sequence indicated by biostratigraphic markers. Parameters used:  $\phi_0 = 0.53$ ,  $\beta = 1.27 \times 10^{-7} \text{ Pa}^{-1}$ .

Sedimentation creates a compaction source term for the fluid overpressuring (Palciauskas and Domenico, 1989). The water overpressure drives an upward hydraulic two-phase flow. Gas is segregated in the sandy formations. The force applied to the gas, which is given by the following (England et al., 1987):

$$\mathbf{F}_g = -(\rho_g - \rho_w)\mathbf{g} - \nabla(\delta p) - \nabla p_c, \quad (29)$$

where  $p_c$  is the capillary pressure. The capillary pressure is given by the Young-Laplace equation:  $p_c = (2/r)\gamma K$  where  $\gamma$  is the interfacial tension of the gas-water interface ( $\sim 72 \times 10^{-3} \text{ Nm}^{-1}$  at  $25^\circ\text{C}$ ),  $r$  is a characteristic length scale that can be interpreted as an effective pore radius for transport in the interconnected pore space, and  $K$  is the “wetting coefficient” usually considered equal to unity. If the formations are perfectly homogeneous,  $dp_c/dz = 0$ . Where there are contrasts in grain size, a differential capillary pressure arises (Berg, 1975), which is given by:

$$\delta p_c = 2\gamma(1/r_2 - 1/r_1), \quad (30)$$

where  $r_1$  and  $r_2$  are the two effective pore radius in the two formations in contact. Gas saturation increases with time at each fine/coarse interface contact. The saturation of gas in the coarse grain formations increases until it reaches such a high value that the gas phase become an interconnected phase (a “gas cap”). When this “critical state” is reached, water cannot flow, and the overpressure increases as more sediments are added to the sedimentary column. The water pressures must exceed the differential capillary pressure and push gas from the coarse to the finest grain-size formations (drainage) before any excess pressure can be dissipated. This is possible only if the fluid overpressure exceed the sum of the capillary pressure drops over the series of interfaces (i.e., the total capillary entry pressure; J. Shosa and L.M. Cathles, unpubl. data). To account for capillary sealing, the Darcy equation must be modified:

$$\mathbf{q}_f = \begin{cases} -\frac{kk_f}{\eta_f}(\nabla\delta p - \nabla p_c), & \text{as } |\nabla\delta p - \nabla p_c| \geq 0 \\ \mathbf{0}, & \text{as } |\nabla\delta p - \nabla p_c| \leq 0 \end{cases}, \quad (31)$$

where  $\mathbf{q}_f$  is the Darcy velocity,  $\eta_f$  is the dynamic shear viscosity of the fluid,  $p_c$  is the capillary pressure,  $k$  is the intrinsic permeability, and  $k_f$  ( $0 \leq k_f \leq 1$ ) is the relative permeability for water, which is a function of the water saturation (Rothman, 1990). Equation 31 is also similar to the equation obtained by Rothman (1990), derived for a two-phase flow in a channel of constant cross section. Equation 31 is supported by numerical and theoretical works (Lenormand et al., 1988; Rothman, 1990) and experimental works (J. Shosa and L.M. Cathles, unpubl. data). Equation 30 shows that the maximum fluid overpressure that a capillary seal (i.e., a permeability barrier associated with sand-shale interfaces in presence of gas caps) can support is equal to the sum of all the capillary pressure differentials inside the seal. We can replace the term ( $\nabla p_c$ ) in Equation 31 by ( $f \delta p_c \mathbf{e}$ ), where  $f$  is the frequency of sand/shale interface which form the capillary seal,  $\mathbf{e}$  is a local unit vector perpendicular to the interfaces and in the direction of the gradient of the capillary pressure, and  $\delta p_c$  is the capillary pressure drop at each interface. A “normal flow” can only be re-established if the excess fluid pressure below the seal exceeds the total capillary entry pressure of the seal ( $f \delta p_c$ ), or if the fracture limit is reached.

At the contact between a clean sand and a clayey sand, a sandy shale, or a shale, the capillary entry pressure is given by (Berg, 1975):

$$\delta p_c = 2\gamma\left(\frac{1}{r_{\text{fine}}} - \frac{1}{r_{\text{coarse}}}\right), \quad (32)$$

where  $r_{\text{fine}}$  and  $r_{\text{coarse}}$  are respectively the characteristic length scales for transport in the interconnected pore space of the fine and coarse grain-size sediments. These length scales can be related to more conventional geometrical parameters by (Revil et al., 1997):

$$r = \frac{2}{3}\left(\frac{d}{\phi^{-m}-1}\right), \quad (33)$$

where  $d$  is an average grain diameter and  $m$  is the electrical cementation exponent,  $m \approx 1.6 \pm 0.2$  for clean sands, and  $2.5 \pm 0.3$  for shales (Revil et al., 1997). Because the specific surface area of an equivalent granular porous media is given by  $V_p/S = (1/6)\phi d/(1-\phi)$ , we can estimate an equivalent grain diameter from the specific surface area data of Patchett (1975) for the different clay minerals. We find the following: kaolinite:  $d = 1 \mu\text{m}$ , illite:  $d = 0.1 \mu\text{m}$ , and smectite:  $d = 1.10^{-2} \mu\text{m}$ . Taking  $\phi = 0.50$ , and the previous values for the grains diameters, the capillary entry pressures for the different clay minerals are the following: kaolinite:  $\delta p_c = 1 \text{ MPa}$ , illite:  $\delta p_c = 10 \text{ MPa}$ , and smectite:  $\delta p_c = 100 \text{ MPa}$ . These values are significant, and consequently capillary sealing could be a very efficient sealing mechanism in sedimentary basins regardless of the value of the intrinsic permeability of the sediments. Equations 32 and 33 can also have been tested using the laboratory experiments of J. Shosa and L.M. Cathles (unpubl. data), who measured experimentally the capillary entry pressure of two artificial sands with very narrow grain-size distributions (2 and 45  $\mu\text{m}$ , porosity 0.45). They found  $\delta p_c = 0.241 \text{ MPa}$  per interface. The application of Equations 32 and 33 leads to  $\delta p_c = 0.237 \text{ MPa}$ , which shows, therefore, a very good agreement between theory and experiments.

Methane was present at all of the sites analyzed. Propane, *iso*-butane, and *iso*-pentane are also present in some formations (for example, between 200 and 450 mbsf at Site 977). At all sites, the origin of most of the methane seems to be biogenic, as indicated by on board headspace gas analysis (Comas, Zahn, Klaus, et al., 1996). We assume that the variation in amount of methane from one hole to another is probably controlled by the concentration of interstitial sulfate, which inhibits methanogenesis in marine sediments (Claypool and Kvenvolden, 1983). For example, at Sites 977 and 979, a biogenic origin of methane is supported by the disappearance of interstitial sulfate at the same depth at which methane concentration begins to rise. High sedimentation rates ensure that organic matter is buried more rapidly than dissolved oxygen can penetrate the sediments from the overlying seawater. In this case, only minor oxic and suboxic degradation of the organic matter occurs, hence fairly reactive organic matter would be preserved. After the sulfate is depleted, methanogenic bacteria degrades the organic matter, producing methane. Consequently, the intensity and depths range of methanogenesis and the sedimentation rate are related. At Sites 979 and 976, the depths of sulfate depletion are 25 mbsf and 24 mbsf, respectively (the sedimentation rates are  $\sim 200 \text{ m/m.y.}$  and  $210 \text{ m/m.y.}$ , respectively), and, in both cases, the concentrations of headspace methane are high. At Site 977, the depth of depletion of sulfate is 46.45 mbsf (the average sedimentation rate is  $\sim 135 \text{ m/m.y.}$  until an unconformity located at  $\sim 500 \text{ mbsf}$  in Hole 977A is reached), and the total headspace methane concentration is high. At Sites 974 and 975, for which the sedimentation rates are low ( $< 100 \text{ m/m.y.}$ ; Figs. 7A, 7B), the overall methane concentration is low (Shipboard Scientific Party, 1996a, 1996b). The interstitial water-sulfate concentrations at these sites indicate that organic-matter degradation occurs mainly by sulfate reduction.

Watts (1987) described two types of capillary seals on the basis of their leaking mechanism. A membrane seal periodically leaks whenever the pore-fluid pressure differential across the seal exceeds the total capillary entry pressure of the seal allowing fluids to enter and pass through the finest grain sized sediments of the seal. Resealing occurs when the pore-fluid pressure drops below the capillary entry

pressure. In the second case, a "hydraulic seal" is formed when the capillary entry pressure is so high that the pore-fluid pressure gradient necessary for fracturing the seal is less than the gradient needed to displace the nonwetting phase through the seal. These two types of capillary seals could explain why fixed and migrating seals are commonly observed in sedimentary basins (A. Revil and L.M. Cathles, unpubl. data). A fixed seal is defined as a permeability barrier attached spatially to a stratigraphic layer during the evolution of a sedimentary basin. A migrating seal is defined as a compartment that migrates in a framework attached to the stratigraphic layers. A complete theory of the dynamics of sealing is investigated by A. Revil and L.M. Cathles (unpubl. data).

In Hole 975C, an increase of porosity is observed below 170 mbsf. Because porosity variations in sedimentary basins are largely irreversible (Palciauskas and Domenico, 1989), this increase of porosity can be only explained as a "frozen porosity" because of the presence of a fixed seal between 145 and 170 mbsf. The presence of this fixed seal is correlated with small-scale lithologic variations in shale content in the same depth range as indicated by the gamma-ray log (Fig. 7A; gamma-ray log). This seal can be classified as a hydraulic seal because the fracture limit for unconsolidated sediment is reached (i.e., zero effective stress). Consequently, the fluid overpressures observed in Hole 975C could be the result of hydraulic seal with a cumulative capillary entry pressure  $>1.4$  MPa (Fig. 7A; fluid overpressure curve) located between 145 and 170 mbsf. About ten layers containing gas are observed at the seal position, which would mean a capillary entry pressure  $>0.14$  MPa per interface, easily obtainable for sediments with the observed sand/shale variations. This seal would have been formed at very shallow depth (below 30 mbsf), as indicated by the magnitude of the "frozen" porosity just below the seal (i.e., at 170 mbsf), in a period of high sedimentation rate (a high sedimentation rate is needed to produce methane at shallow depths, and is observed in Fig. 1 at the depth corresponding to the top of undercompaction, 154–178 mbsf).

In all the other holes analyzed, the porosity trend in the undercompacted formations is nearly a constant. This is typical of a migrating seal because the uniform porosity in these compartments requires a constant effective stress (porosity is a linear function of the effective stress, see Eq. 3). Consequently, the downward increase in pore-fluid overpressure is balanced by the downward increase in lithostatic load. This is possible only if the depth of the migrating seal remains fairly constant (i.e., the migrating seal moves in a framework attached to the geological formation sediments). In this case, there is a dynamic equilibrium between capillary and fluid overpressure forces of the seals that is maintained at the same depth over time. Sealing in these holes can be classified as membrane seal. It is striking to observe that the depth corresponding to the top of the overpressured section is always in the range 100–120 mbsf (except at Site 975 where a fixed seal is observed). This depth could be related to the bubble point of methane. The stability and the thermodynamic properties of methane in sedimentary basins are discussed by Brown (1990, and references therein).

## CONCLUSIONS

Fluid overpressures observed in sediments cored in the Western Mediterranean Sea during Leg 161 are explained as the result of disequilibrium compaction associated with the presence of free methane, high sedimentation rates, and the alternating layers of coarse and fine grain sediments. Most of the methane is probably formed by in situ microbial degradation of the organic matter present in the sediment. We have shown that capillary phenomena can produce capillary seals at the sites investigated during Leg 161. These seals are fixed or migrating in a framework attached to the sedimentary layers.

A general theory of compartmentalization and sealing will be published elsewhere and applied to these data to understand the dynamics of these seals.

## ACKNOWLEDGMENTS

We would like to thank Larry Cathles, Jennifer Shosa, Yves Bernabé, and Steve Losh for stimulating discussions and advice. This paper has benefited greatly by the critical reviews of Philip Stauffer and William Ussler.

## REFERENCES

- Bangs, N.L.B., Westbrook, G.K., Ladd, J.W., and Buhl, P., 1990. Seismic velocities from the Barbados Ridge Complex: indicators of high pore fluid pressures in an accretionary complex. *J. Geophys. Res.*, 95:8767–8782.
- Berg, R.R., 1975. Capillary pressures in stratigraphic traps. *AAPG Bull.*, 59:939–956.
- Bradley, J.S., and Powley, D.E., 1994. Pressure compartments in sedimentary basins: a review. In Ortleva, P.J. (Ed.), *Basin Compartments and Seals. AAPG Mem.*, 61:3–26.
- Brown, K.M., 1990. The nature and hydrogeologic significance of mud diapirs and diatremes for accretionary systems. *J. Geophys. Res.*, 95:8969–8982.
- Cathles, L.M., and Smith, A.T., 1983. Thermal constraints on the formation of Mississippi valley-type lead zinc deposits and their implication for episodic basin dewatering and deposit genesis. *Econ. Geol.*, 78:983–1002.
- Claypool, G.E., and Kvenvolden, K.A., 1983. Methane and other hydrocarbon gases in marine sediment. *Annu. Rev. Earth Planet. Sci.*, 11:299–327.
- Comas, M.C., Zahn, R., Klaus, A., et al., 1996. Proc. ODP, Init. Repts., 161: College Station, TX (Ocean Drilling Program).
- Deer, W.A., Howie, R.A., and Zussman, J., 1966. *An Introduction to the Rock-Forming Minerals*: London (Longman Group).
- Ellis, D.V., 1987. *Well Logging for Earth Scientists*: New York (Elsevier).
- England, W.A., Mackenzie, A.S., Mann, D.M., and Quigley, T.M., 1987. The movement and entrapment of petroleum fluids in the subsurface. *J. Geol. Soc. London*, 144:327–347.
- Fertl, W.H., 1976. *Abnormal Formation Pressures*: Amsterdam (Elsevier).
- Fowler, W.A., 1970. Pressures, hydrocarbon accumulation and salinities: Chocolate Bayou field, Brazoria County, Texas. *J. Pet. Tech.*, 22:411–423.
- Hamilton, E.L., 1971. Elastic properties of marine sediments. *J. Geophys. Res.*, 76:579–604.
- Lenormand, R., Touboul, E., and Zarcone, C., 1994. Numerical models and experiments of immiscible displacements in porous media. *J. Fluid Mech.*, 189:165–187.
- Magara, K., 1978. *Compaction and Fluid Migration: Practical Petroleum Geology*, Dev. Pet. Sci., 9. Amsterdam (Elsevier).
- Maxwell, J.C., 1964. Influence of depth, temperature, and geologic age on porosity of quartzose sandstone. *AAPG Bull.*, 48:697–709.
- Palciauskas, V.V., and Domenico, P.A., 1989. Fluid pressures in deforming porous rocks. *Water Resour. Res.*, 25:203–213.
- Patchett, J.G., 1975. An investigation of shale conductivity. SPWLA, 16th Ann. Logg. Symp., Pap. U.
- Revil, A., Pezard, P.A., and Darot, M., 1997. Electrical conductivity, spontaneous potential and ionic diffusion in porous media. In Lovell, M.A., and Harvey, P.K. (Eds.), *Developments in Petrophysics*, Geol. Soc. Spec. Publ. London, 122:253–275.
- Ross, B., 1990. The diversion capacity of capillary barriers. *Water Resour. Res.*, 26:2625–2629.
- Rothman, D.H., 1990. Macroscopic laws for immiscible two-phase flow in porous media: results from numerical experiments. *J. Geophys. Res.*, 95:8663–8674.
- Shi, Y., and Wang, C.-Y., 1988. Generation of high pore pressures in accretionary prisms: inferences from the Barbados Subduction Complex. *J. Geophys. Res.*, 93:8893–8909.

- Shipboard Scientific Party, 1996a. Site 974. In Comas, M.C., Zahn, R., Klaus, A., et al., *Proc. ODP, Init. Repts.*, 161: College Station, TX (Ocean Drilling Program), 55–111.
- Shipboard Scientific Party, 1996b. Site 975. In Comas, M.C., Zahn, R., Klaus, A., et al., *Proc. ODP, Init. Repts.*, 161: College Station, TX (Ocean Drilling Program), 113–177.
- Shipboard Scientific Party, 1996c. Site 977. In Comas, M.C., Zahn, R., Klaus, A., et al., *Proc. ODP, Init. Repts.*, 161: College Station, TX (Ocean Drilling Program), 299–353.
- Shipboard Scientific Party, 1996d. Site 979. In Comas, M.C., Zahn, R., Klaus, A., et al., *Proc. ODP, Init. Repts.*, 161: College Station, TX (Ocean Drilling Program), 389–426.
- Steenhuis, T.S., Parlange, J.-Y., and Kung, K.-J., 1991. Comment on “The diversion capacity of capillary barriers” by Benjamin Ross, *Water Resour. Res.*, 27:2155–2156.
- Watts, N.L., 1987. Theoretical aspects of caprock and fault seals for single- and two-phase hydrocarbon columns, *Mar. Pet. Geol.*, 4:274–307.

**Date of initial receipt: 23 May 1997**

**Date of acceptance: 19 December 1997**

**Ms 161SR-274**